TEMPERATURE MEASUREMENTS OF A MARTIAN LOCAL DUST STORM

Ralph Kahn

Jet 'repulsion Laboratory / California Institute of Technology

ABSTRACT

A technique for estimating the ground and near-ground atmospheric temperatures within a martian local dust storm is presented, It is applied to soundings taken by the Viking Orbiter Infrared Thermal Mapper (IRTM) instrument at 4 times-of-day for one storm, Essentially, a comparison is made between infrared radiances emerging from the storm interior and those from the region surrounding the storm. Particle extinction proper-ties are assumed to be independent of position in the storm region, and scattering properties must be selected arbitrarily. For the storm studied here, the ground temperature in the interior is at least 6K cooler, whereas the mar-ground atmospheric temperature may be less than or comparable to, those of the surroundings. The thermal structure of the storm interior did not change measurably between 11.5 and 16.6 local hours. These observations favor theories of dust storm development in which regional winds rather than local, dust-driven convection initiate the mobilization of dust from the surface. In addition, optical properties obtained for the dust particles in this storm differ from those observed by Mariner 9 during the 1971-2 global dust storm,

1.   INTRODUCTION

Although the occurrence of local and regional dust storms on Mars is well-documented (Briggs et al.. 1979; Peterfreund and Kieffer, 1979; Zurek , 1982), there is still some question as to the means by which dust is initially mobilized at the martian surface (e.g., Greeley et al. 1992). The idea that regional winds superimposed on the general circulation provide the shear stress necessary to lift dust at the surface is supported both by theory and observation (Leovy et al. 1973; Zurek et al. 1992). Similarly, there is evidence that direct heating of the surface creates free convective vortices that mobilize dust locally as dust devils (Gierasch and Goody, 1973; Ryan and Lucuch, 1983; Thomas and Gierasch, 1985). Constraints on the evolution of temperature within martian local dust storms would provide important clues as to the mechanisms that operate under different environmental conditions on Mars.

This paper demonstrates a technique that places some very crude but relevant constraints on the temperatures of martian local dust storms. The method relies on broad-band infrared soundings from the Infrared Thermal Mapper (IRTM) experiment flown on the Viking Mission to Mars. The IRTM made observations over an extensive part of the planet, covering a wide

range of seasons and local conditions. Although four of the five detector channels were designed to examine surface emissions (Kieffer et al. 1972), the substantial infrared opacity of the dusty martian atmosphere, even during relatively clear conditions, produced a measurable atmospheric contribution to the observed infrared radiances (Kieffer et al. 1977). These data represent the most detailed and extensive spatial and temporal record of the martian atmosphere yet available. In particular, IRTM data includes observations made during the development of a few local dust storms (Peterfreund and Kieffer, 1979). Thermal signatures at these sites show distinct spectral characteristics that contain information about the thermal behavior of the storms.

Current knowledge of infrared absorption and scattering properties of particles in the Martian atmosphere, the surface emission properties, and our understanding of the vertical distribution of opacity in the Martian sky, are limited. Interpretation of broad-band radiances, which sample the surface together with the lower atmosphere, is therefore only partly constrained by existing data. This paper explores a number of the most reasonable hypotheses about the atmospheric optical and thermal structure for consistency with the IRTM observations over a dust storm. The technique essentially makes a comparison between infrared radiances emerging from the storm interior and those from the area surrounding the storm. Data from the Viking Lander 1 (VL1) site is also examined.

The paper begins by presenting the IRTM data used in this study, and the model used to simulate lRTM spectra. Then the thermal signatures of an area adjacent to a local dust storm are examined. In the dust storm surroundings, the vertical temperature strucutre is easier to constrain than in the interior. IRTM soundings in the surroundings are used to obtain ratios of particle extinction optical properties from constraints on the temperature structure. Particle scattering properties must be selected arbitrarily for this calculation, but we can place sufficient constraints on the atmospheric opacity and vertical temperature structure to obtain meaningful extinction coefficients. Next, an attempt is made to calculate the mean atmospheric infrared spectral extinction over the VL1 site, as was done in the dust storm surroundings. However, the low atmospheric opacity at the VL1 site makes the inversion particularly sensitive to the unknown ground temperature and emissivity. Finally, particle properties arc assumed to be independent of position in the storm region. With the help of the constraints on particle properties from the storm surroundings, IRTM soundings of the storm interior are used to obtain an effective dust cloud temperature and the ground temperature at the storm center.

The results of these studies represent a step toward constructing thermodynamic models of dust storm generation and growth. The data examined in this paper arc of low surface

resolution, so it is not possible to perform critical tests on length scales small enough to rule out either of the proposed dust storm mechanisms. However, this work establishes the viability of a technique that can be applied to data with higher spatial resolution.

2. IRTM DUST STORM DATA

The data used in this study were taken by the Viking Orbiter IRTM experiment in four broad-band channels centered near 7,9, 11, and 20 microns. The IRTM channel passbands are given in figure 1. The 7,9, and 11 micron bands are each about two microns wide. The 20 micron band is nearly 6 microns wide. Following conventions established in earlier presentations of IRTM data (see e.g., Kieffer, et al. 1977), the observed radiances are given in terms of brightness temperatures T_7, T_9, T_{11}, ancl T_{20}, measured in the bands centered near 7, 9. 11, and 20 microns, respectively.

The IRTM instrument made 28 simultaneous soundings: four measurements directed at each of seven spots on the surface. The instrument contained four telescopes. Each telescope sampled light from all seven spots, and focused this radiation onto seven detectors. The telescopes were aimed so that the same seven surface locations, labeled spots one to seven, were observed by each telescope. One telescope served seven 20 micron detectors, another provided light for seven 11 micron detectors, so there is an 11 micron and a 20 micron measurement for every spot in the IRTM data. A third telescope made seven albedo measurements, which arc not used in this study. The fourth telescope had three 7 micron detectors, three 9 micron detectors, and one 15 micron channel to measure atmospheric emissions. Therefore, simultaneous 7 and 9 micron measurements cannot occur at any spot. For this reason all the spectral measurements used here are compared with the 11 micron data, which was obrained for every location. Further details of the IRTM are given in Kieffer et al. 1977.

A local dust storm that occurred in the Solis Planum region of Mars during summer in the sout hem hemisphere ($L_S = 227$) was selected for this study. The storm appeared in four separate sequences of IRTM observations on the same day, between 11.5 hours and 16.6 hours local time (Peterfreund and Kieffer, 1979). The orbiter camera recorded a dust cloud in this region on the subsequent day. Figure 2 illustrates the dust storm data. Each graph contains the spectral brightness temperature differences along an cast to west traverse, transacting the region of the storm with the most pronounced temperature differences relative to the surroundings. Spectral temperature differences are calculated from pairs of observations with the same telescope spot number, to minimize sampling errors in regions of large thermal contrast. Although brightness

3

temperature values exhibit a 3K to SK scatter for adjacent measurements, temperature differences taken in this way are consistent to better than 1 K in most instances. Some sampling error does occur since for fixed temperature, the slope of the Planck function depends on wavelength. This causes the spectral detectors to have varying sensitivity to thermal inhomogeneity in the field of view (Martin et al. 1979; Jakosky, 1997). The spatial resolution on the martian surface of the four sequences shown lies between 220 km and 230 km.

Data were selected within a three-to-four-degree strip centered about the latitude shown, so the centers of the sampling circles are within 180 to 240 km of the latitude of the traverse. The physical size of the dust storm, as judged from the perturbation of the temperature in IRTM contour maps (Peterfreund and Kieffer, 1979) is about 450 km by 850 km. This size is comparable to that of the cloud photographed in the same region on the following day by the orbiter cameras. In summary, the available data averages out any thermal features with length scales less than two hundred kilometers, and there are three to four resolution elements across the storm itself.

The accuracy of the brightness temperatures varies among the channels. The absolute errors are less than 0.5K in the T_7, T_9, T_{11}, and T_{20} bands for the temperature ranges considered here, according to Kieffer et al. (1977).

'l'he storm center is taken to be at the T_{11} minimum. In figure 2, note that $T_7 - T_{11}$ reaches a maximum near the storm center. In three of the traverses, $T_9 - T_{11}$ has a maximum near the storm center, whereas $T_{20} - T_{11}$ shows a relative minimum. The temperature differences are asymmetric about the extremes, with a considerably steeper gradient in $T_\lambda - T_{11}$ to the east of the storm center, and a progressively shallower slope to the west for later measurements, except for $T_{20} - T_{11}$ in the fourth sequence. From these data, representative models of the dust storm center and surroundings were constructed, to be used in the numerical simulations. These are presented in table 1. For this storm, the brightness temperatures decrease about 35 deg, the $T_7 - T_{11}$ and $T_9 - T11$ contrasts increase, whereas $T_{20} - T_{11}$ decreases in the dust storm interior relative to the surroundings.

3.   NUMERICAL SIMULATION OF SPECTRA

Synthetic spectra were produced for comparison with the IRTM data using a two-stream , radiative transfer model similar to that of Toon et al., 1977. The work of Toon et al. is an analysis of data from the infrared interferometer spectrometer (IRIS) that flew on the Mariner 9 Mission to Mars. The instrument obtained high-resolution spectra from 5 to 50 microns.

Vertical temperature profiles were calculated from separate analysis of CO_2 bands in the IRIS data. "l'he dust model required input values of the ground temperature, the optical depth at one wavelength, and the particle extinction and scattering properties. Toon et al. assumed spherical particles, and let the real and imaginary parts of the index of refraction at each wavelength, as well as the particle size distribution, be free parameters giving the particle scattering properties in their model. They obtained particle indices of refraction, size distribution, and atmospheric optical depth at each wavelength by comparing the model results with the IRIS data. The data anal yzed by Toon et al. were taken during the martian global dust storm of 1971 -72., when the atmospheric dust loading was near its maximum.

For the present study, source functions were obtained at all levels using upward and downward intensities calculated from the two-stream equations. This method was selected because it is the simplest one that includes the two parameters describing martian dust properties for which constraints are avaliable. It also allows direct comparison with the results of Toon et al. The technique approximates the angular dependence of the radiation field due to scattering anisotropy by taking average values in two directions over the sphere. To obtain the emergent intensity, the source function in the upward direction is integrated along the path selected by the viewing angle, thereby preserving the geometrical angular dependence of the result. The method of solution differs from that of Toon et al. in that here the equation for the upward two-stream intensity is written as a second order differential equation with two-point boundary values, solve using a standard numerical method (Lindzen and K uo, 1969), and subsequently obtain the downward two-stream intensity as an initial value problem using a Runge-Kutta method of order three. Details of the calculation are given in the appendix. The procedure was tested by calculating the examples given in Toon et al., and obtaining the same results to two significant figures or better.

Unlike the high-resolution IRIS data, this study relies on broad-band observations, with a direct measurement of the atmospheric temperature at only one level, near 24 km, as obtained from the IRTM 15 micron channel. The particle scattering properties at each wavelength are given by two parameters, the single scattering albedo $(\tilde{\omega}_0)$ and the integral of the normalized single scattering phase function weighted by the cosine of the scattering angle, which is called the asymmetry factor (β). These parameters cannot be determined from the IRTM data; initially, they are assumed to be equal to those derived by Toon et al. The sensitivity of the results to small changes in these values is examined later. Vertical temperature structure, spectral opacity, and ground temperature are free parameters, as discussed below.

To produce a model spectrum, the ground temperature, the atmospheric thermal profile, the vertical distribution of opacity, the spectral extinction coefficients $Q_e(\lambda)$, the scattering parameters $\omega_0(\lambda)$ and $\beta(\lambda)$, and the surface emissivity must be specified. The model allows arbitrary selection of vertical temperature structure. It is parameterized here by the ground temperature T_g, the atmospheric temperature at the ground 1'., the boundary layer height Z_{BL}, and boundary layer lapse rate Γ_{BL}, the atmospheric lapse rate I"$_a$, and the height of the tropopause Z_{trop}, above which the temperature is taken to be independent of height. These quantities are illustrated in figure 3(a). Figure 3(b) shows the thermal structure used for dust storm interior models, which are discussed in a later section. The emission angle for most of the dust storm observations used in this study lies between 30 and 45 degrees; this parameter is set to 35 degrees for most of the models. This happens to be the angular region in which the two-stream method most closely approximates detailed radiative transfer calculations for expected particle size distributions (Toon et al. 1977). The calculated spectral brightness temperature differences vary less than one degree for changes of at least 5 degrees in the input emission angle . around the nominal value selected.

4.   MODELS OF THE DUST STORM SURROUNDINGS

We seek information about atmospheric and ground temperatures in the interior of a dust storm. The general radiative transfer problem requires a knowledge of both the particle properties and the vertical temperature structure. Reasonable estimates of some of the particle properties can be obtained using an assumed vertical temperature in the dust storm surroundings. Some parameters in the temperature profile of the storm interior can then be retrieved using the deduced particle properties. In this section, the ratios of the spectral extinction coefficients required to reproduce the observed spectra for the dust storm surroundings are calculated. These results will depend upon the unknown vertical temperature structure in the dust storm surroundings, so a range of possible values is obtained for the spectral extinction coefficients, based upon different choices of T_g, To, and Γ_{BL}. However, with the available data, reasonable limits are placed on the values of these parameters in the storm surroundings. Extinction coefficients are represented as ratios $R = Q_\lambda / Q_{i}1$, where Q_λ is the extinction coefficient in the wavelength band λ, which may be 7, 9, or 20 microns, and Q_i1 is the extinction coefficient in the 11 micron band. For each assumed temperature profile, three ratios of extinction coefficients are calculated, together with a value of the optical depth at 11 microns, to match the four observed brightness temperatures.

Since the ratios of extinction coefficients are less dependent on the assumed temperature profile than are the opacities at each wavelength, these ratios are retrieved for later use in the dust

storm interior models. For the interior models, the 11 micron dust cloud opacity (τ_{11C}) is treated as a free parameter. With these inputs, and the observed spectrum at the storm center, values of T_g and the effective dust cloud temperature T_C are constrained using a least-squares scheme.

Figure 4 shows the results of numerical modeling of the dust storm surroundings. The choice of parameter space and sensitivity of the results to each of the parameters is now discussed. 'I'he uncertainty in R_λ is primarily due to the indeterminacy of T_g. T_g was varied from 288K to 292K. Near midday, and where the atmospheric visible opacity is less than 1, T_g is expected to be greater than the atmospheric temperature, based on theoretical modeling (Gierasch and Goody, 1972; Pollack et al. 1979). The largest observed brightness temperature in the dust storm surrounding is 286 K, which is therefore a lower bound on the choice of T_g. I'he upper bound on T_g in the parameter space is arbitrary. A reasonable guess at an upper bound on T_g is made by noting that T_g is a sensitive function of the 11 micron atmospheric opacity. There is no direct measurement of the 11 micron optical depth, but the visible optical depth in the dust storm surroundings is typically less than 1, as evidenced by the appearance of ground features in the orbiter images of local dust storms (Briggs et al., 1979), including one taken in the same region as the storm used in this study, on the subsequent clay.

Next, the 11 micron opacity needs to be related to the estimated visible opacity. The relative particle extinction cross sections for martian dust in the visible and infrared regions is not yet well-established (Zurek, 1982). Pollack et al. (1979) use visible properties obtained from the Viking lander camera experiments and infrared properties derived from the Mariner 9 IRIS measurements, thereby assuming that the atmospheric particles are the same in these two situations, Using these data, the 11 micron opacity would be less than the visible opacity. Unfortunately, we later conclude that the particle properties observed over the dust storm must differ from those of the Manner 9, so we have no way to make a direct comparison between visual and 11 micron opacities, which would set a firm upper bound on the value of T_g. However, the infrared extinction cross sections for micron-sized dust particles are typically smaller than the visible extinction cross sections. Therefore, values of T_g were selected for which the 11 micron opacity is less than one. The chosen range of "I'$_g$ values results in a 30% uncertainty in R_7, and smaller uncertainties in R_9 and R_{20}.

The surface emissivities were all chosen to be equal to 1. For the most probable surface materials, the 7 micron emissivity will be near 1 (Martin et al., 1979), whereas emissivities in the 9, 11, and 20 micron bands will be more dependent upon surface composition and structure, and may be as a low as 0.85 for some likely situations (Kieffer et al., 1972; Conel, 1969). However,

the ground temperature affects the radiance in the"] micron band more than the other bands. The 10-to-1 5 percent uncertainty in surface emissivity can contribute as much as a 10% error to the derived extinction coefficient ratios, particularly R_7. It is more likely that the 9 ant] 11 micron emissivities, if less than 1, are within a few percent of each other, so that R_9 will exhibit smaller errors.

Values of T_O (see figure 3a) are taken to fall between 220K and 260K, which covers the range of possible values consistent with radiative-convective modes of the martian atmosphere in the afternoon at mid latitudes (Gierasch and Goody, 1972; Pollack et al., 1979). These models were confirmed to a limited degree by values of T_O measured at the Viking lander sites by the Viking meteorology experiment (Hess et al., 19"/9). The upper limit to this range is also determined by limiting the value of $\tau 11$ to unity. The boundary layer height was varied between 3 and 8 km, and adiabatic (4.5 deg/km) and isothermal lapse rates in the boundary layer were chosen as limiting cases; The range of boundary layer height includes the theoretical boundary layer thicknesses in the afternoon (Gierasch and Goody, 1968; Pollack et al., 1979), and covers the dust cloud height estimates made from Viking imaging and infrared data (Peterfreund and Kieffer, 1979). The atmospheric lapse rate above the boundary layer was determined by fixing the atmospheric temperature at 24 km to be a 200K, as measured by the 15 micron channel of the IRTM instrument in the region of the storm observation (Martin and Kieffer, 1979). An exponential vertical distribution of opacity, with a scale height of 10 km, was used for all models of the dust storm surroundings, to match the results obtained from Viking Lander Imaging experiments (Kahn et al., 1980). This implies that the dust is well-mixed in the lower atmosphere. For exponential vertical distributions of opacity, the results are not noticeably affected by the choice of tropopause height, since only a few percent of the total radiation comes from the atmosphere above 20 km in these models. For example, the deduced ratios of extinction coefficients vary less than 2.5% when the tropopause is moved from 50 to 64 km, for a model with other inputs set in the middle of the parameter space.

Figure 4 presents a series of model results covering the parameter space discussed above. For all cases, mean values of@ and β weighted by the Planck function are used, as obtained for the particles observed by the Mariner 9. This assumption is discussed subsequently. The weighted average of property A at temperature T is defined. as:

$$\overline{A}_i = \int A(\lambda) B(\lambda, T) f_i(\lambda) d\lambda / \int B(\lambda, T) f(\lambda) d\lambda \qquad (1)$$

where $B(\lambda, T)$ is the Planck function at temperature T and fi (λ) is the relative IRTM response for band i at wavelength λ, given by Kieffer et al. (1977). Values of the dust particle parameters calculated in this manner are shown in table 2. From figure 4, τ_{11} increases with To, but the ratios R_λ are virtually independent of To and Γ_{BL}. Q_7 depends heavily on the choice of T_g, whereas R_9 and R_{20} are much less affected. 'I'his confirms that the 7 micron channel samples the ground much more than the other channels, as was indicated by the highe observed brightness temperatures at 7 microns by the IRTM instrument. Table 3 presents the range of values of the extinction coefficient ratios deduced from figure 4. For comparison, the ratios of extinction coefficients for the particles observed by Mariner 9 (Toon et al., 1977) are also given in table 3, and are plotted as circles in figure 4. The derived extinction coefficient ratios are not consistent with those of the Mariner 9 particles. Note that by increasing T_g abov 292K, R_7 can be made to fit, but then R_9 would exhibit an even poorer fit to the Mariner 9 data. Other evidence that the properties of martian atmospheric dust particles vary in space and time have appeared in several sources (Clancy and Lee, 1991; Kahn et al, 1992).

The values of ω_0 and β were assumed to be equal to those of the Mariner 9 particles. There is insufficient information to make a direct determination of these values from the Viking data. The particle scattering properties are treated as free parameters in this study, avoiding the questions of particle composition and size distribution. The sensitivity of the conclusions to these choices is tested below. A number of perturbation studies were also performed on the values of ω_0 and β, although there is no formal basis on which to limit the choices. For 10% changes in ω_0 and β, we obtain less and a 5% change in the derived value of Q_7, a 1070 change in Q_9 and Q_{11}, and less than a 3% change in Q_{20}. One alternative to this approach is to vary the particle composition and possibly the size distribution to obtain particl optical parameters which yield agreement between the model and the observed spectra. This approach has been employed by Hunt (1979), who concludes that the thermal signature of a dust cloud is reproduced using dust composed of two common terrestrial minerals, with the same size distribution as the Mariner 9 particles. However, this result relies on specific assumptions about the temperature structure, and especially upon the particle size distribution and allowed composition of the particles. (1/or example, water ice was not included as a possible contributor to the column opacity.) These assumptions are of necessity arbitrary sine there are only four directly-measured quantities in the problem. 'I'he introduction of an additional free parameter increases the difficulty in extracting valid information from the model.

The derived ratios of extinction coefficients are model-dependent, particularly with regard to the assumed scattering properties of the particles. The most likely values of R_λ, based

on a wide range of possible thermal conditions, are given in table 3. In summary, for all reasonable thermal profiles, the observed particle properties differ from those of the Mariner 9 dust. Given the arbitrary assumption that the particle scattering properties are similar to the Mariner 9 dust, this approach sets useful limits on the ratios of extinction coefficients from the IRTM data.

5.   VIKING LANDER 1 SOLO MODELS

The best available constraints on martian atmospheric structure were acquired over the Viking Lander 1 (VL1) site at the time of the VL1 entry (Sol O). The vertical temperature profile was measured direct] y by probes on the entry vehicle (Sieff and Kirk, 1977), and the vertical distribution of opacity locall y from Lander Camera experiments (Kahn et al., 1980). "l'his appears to be an ideal place to test the. procedure for retrieving particle extinction properties from IRTM data that was presented in the previous section. With the ac'ditional information, the particle properties would seem to be better determined than for the dust storm surroundings case. However, the unknown surface emissivities, ground temperature, and particle scattering properties are still required for the model. The atmospheric visible opacity is more than a factor of two lower at the VL1 site than in the dust storm surroundings, based on imaging data. The differences between brightness temperature values in the IRTM channels are much smaller at VL1 than in the dust storm surroundings. This is a manifestation of the lower optical depth at the VL1 site, where most of the observed radiation comes directly from the ground to the IRTM detector.

In table 4 the IRTM observations which most closely correspond to the VL1 site at Sol O are listed, The landing occurred at 16.13 local time. Column 1 of table 4 shows the orbiter revolution and sequence identification number. Columns 2, 3, and 4 contain the mean viewing angle of the observation, the approximate local time of day, and the surface resolution of the observations. 'l'he subsequent columns show the mean and standard deviation of the IRTM 11 micron brightness temperature and the "1'$_7$- T$_{11}$, T$_9$ - T$_1$1, and T$_{20}$- T$_{11}$ differences. For each IRTM sequence, all the data in a one-degree box around the landing site has been accumulated, and the brightness temperature differences were calculated using pairs of measurements made simultaneously for the same telescope spot number. From these data, a representative thermal signature was abstracted (table 5), to be compared with synthetic spectra. These results are modeled using a temperature profile with To $=$ 24 1.5K, the top of the boundary layer at 7.5 km with temperature 215.95K, and a 140K tropopause at 57.5 km (Sieff and Kirk, 1977). The scale height for opacity is set at 10 km. There is no direct measurement of T$_g$, since the ground temperature sensor is partly shaded during the afternoon (Moore et al., 1977). values of Tg

bet ween 248K and 258K are expected, based on theoretical modeling (Pollack et al., 1979; Moore et al., 1977).

The results are shown in figure 5. For comparison, particle extinction ratios for Mariner 9 observations are given as symbols in the diagram. The average particle proper-tics required in the vertical column over the VL1 site as deduced from this calculation differ from both the Mariner 9 particles and the properties deduced for the dust storm area (figure 4). There are many possible reasons for the difference in calculated particle properties. These include differences in particle composition and size distribution, differences in surface emissivity, and the possible presence of additional constituents in the vertical column, as for example, water ice haze. The VL1 site results are also much more susceptible to errors in the data, since the observed spectral temperature differences here (less than 2K) are much smaller than in the dust storm surroundings cases (4K to 1 1K).

The calculations in figure 5 assume ω_0 and β to bc the same as their Mariner 9 values, and the spectral emissivity of the surface was set to 1. The total atmospheric opacity at the VL1 site is smaller than in the dust storm area, so the ground emissivity for this case has a much greater effect on the net radiance at the detector than in the previous calculations. Examination of the surface rocks at the VL1 site suggest basaltic composition (Binder et al., 1977). If the surface in the vicinity of the lander is composed of basalt, the average surface emissivity in each of the IRTM bands is expected to range between 0.9 and 1.0 (Hovis and Callahan, 1966). However, the emissivity for pure solid basalt reaches a minimum of about 0.83 near 10 microns, which will contribute to the 9 and 11 micron bands to varying degrees, depending on the size of the surface particles. The 7 micron emissivity is 0.97 or greater for particles larger than 0.105 mm. These data suggest that R_7 may be higher than is shown in figure 5 if the surface is composed of pure basalt. No conclusion can be drawn regarding R_9. Reasonable assumptions about surface materials could produce temperature differences on the order of those observe d in the IRTM spectrum. In summary, the particle extinctions derived from the information currently available at the Viking Lander 1 site are likely to bc seriously affected by the arbitrary choice of T_g and surface emissivit y.

6.   THE DUST STORM INTERIOR

Using the range of particle properties deduced in the dust storm surroundings, we now construct a model of the atmosphere at the dust storm interior. The dust cloud is treated as a boundary layer phenomenon, with a characteristic temperature T_C and an optical depth at 11 microns τ_{11C}. Above the cloud, the vertical structure of the atmosphere is assumed to be similar

to the surroundings, and unaffected by the presence of the cloud. This structure is illustrated in figure 3b. The 1 5 micron brightness temperature measurements, which sample at about 24 km above the surface, are unaltered by the presence of the dust cloud (Peterfreund and Kieffer, 1979). Visible images of local dust clouds also exhibit sharp upper boundaries (Briggs et al., 1979). In addition, observed radiances are heavily weighted to the more optically dense lower atmosphere even in the dust storm surroundings, as discussed in Section 4. Since the dust cloud has a larger opacity than the boundary layer of the dust storm surroundings, the contribution of the atmosphere above the cloud top to the. total radiance will not have an important effect upon the results.

The temperature structure for dust storm interior model contains two parameters, T_g and T_c, that are fit in the least- squares sense by the four spectral radiances obtained over the dust storm interior (see figure 3b). For this procedure to be meaningful, the four atmospheric weighting functions must overlap in the region of the cloud, since there is only one free parameter in the vertical temperature profile above the ground. Knowledge of the vertical distribution of opacity within the cloud is insufficient to justify a more elaborate temperature structure model. The atmospheric weighting functions must also be insensitive to the rest of the atmospheric structure, and must sample the ground relative to the cloud to varying degrees. "l'he last two properties are strongly suggested by the results shown in figure 4, and can be checked post-hoc by the convergence and stability of the least-squares procedure. From figure 4, Tg is the most sensitive to the value of T_7, whereas of all the channels, the response of T_0 is greatest to changes in T_{20}. The relative independence of the atmospheric contribution to the measurements can be evaluated by calculating the overlap integral of the weighting functions which is a measure of the coincidence of the regions sampled by any pair of channels:

$$W_{i,j} = \left| 1 - \int_0^\infty K_i\, K_j\, dz \Big/ \int_0^\infty K_i^2\, dz \right|$$

where Ki is the derivative of the transmission function for spectral band i (e.g. Rogers, 1976). This quantity is equal to zero if the two channels sample exactly the same vertical region of the atmosphere, and approaches one if the channel sampling functions do not overlap. For $W_{i,j}$ between about 0.0 and 0.3, $1 - W_{i,j}$ is approximately equal to the fractional overlap of the two-channel sampling functions in these models. in the. dust storm surroundings, the distribution of opacity leads to values of $W_{i,j}$ which range between 0.16 and 0.3, given the models in section 4. Thus the overlap of sampling functions is very high. increasing the optical depth in the boundary layer, to simulate a dust cloud, produces values of $W_{9,11}$, $W_{1,20}$, and $W_{9,20}$ between 0,20 and

0.25. These three channels sample the atmosphere at nearly the same level. Overlap with the 7 micron channel may be as small as 50% for some models. This channel samples closer to the ground than the others, and also receives a larger proportion of net radiation from the ground itself. By calculating one representative atmospheric temperature in the inversion scheme, in addition to the ground temperature, the value of T_g will be aliased if the cloud is not isothermal. However, this effect is small, as is shown in the discussion of perturbation studies below.

Figure 6 illustrates the least-squares solution to T_g and T_c for the dust storm interior as a function of τ_{11C}. The particle properties obtained for the dust stern-r surroundings, as given in table 3, have been used. The vertical dust distribution is discontinuous, with the cloud top set at 4 km, and the scale height of dust set 10 km in both the cloud and in the atmosphere above. The 11 micron opacity of the atmosphere above the cloud is fixed at 0.4, which is equal to the 11 micron atmospheric optical depth above 4 km in the middle of the parameter space for the dust storm surrounding models. The atmospheric temperature at the cloud top is taken as 220K, and the atmospheric lapse rate is determined so that at 24 km the temperature is 200K, to agree with the IRTM measurements at 15 microns (Martin et al., 1979), as was done in the cloud free area. Convergence is achieved to better than 1 degree per channel, which is comparable to the experimental accuracy of the IRTM, for τ_{11C} less than 3. Solutions are less accurate for large cloud opacity, and for $\tau_{11C} = 5$ the least-squares solution for T_9 deviates by 5 degrees from the observed value.

In figure 6, the T_g below the dust cloud is less than 280K for all choices of τ_{11C}. For the dust storm surroundings model, the absolute lower bound on T_g came to 286K. The value of T_C is less certain, and depends strongly on the value of t_{11C}. In particular, T_C varies most rapidly when $\tau_{11C} < 3$. This is explained as follows: from figure 4, T_g is most sensitive to the value of T_7, and in table 3, the ratio of extinction coefficients for the 7 and 11 micron bands is about one third. So when τ_{11C} is increased to 3, the 7 micron opacity reaches unity, and the ratio of ground to atmospheric radiation becomes less dependent upon τ_{11C}. No specific conclusions can be drawn about the effective temperature of the dust cloud as related to the boundary layer temperature in the surroundings because of the large uncertainty in both these quantities. Theoretical modeling of the boundary layer temperature in the mid afternoon at a similar latitude in the northern hemisphere, for early summer, yields temperatures near 230K (Pollack et al., 1979). The increased visual optical depth (which is still less than one) and the greater solar input in the dust storm surroundings over those of the VI,1 site models can raise this temperature on the order of 10K (figures 7 and 8 in Pollack et al., 1979). This places the current estimate of the near-ground temperature at the upper end of the range of possible values of T_C. From these

results, note that $T_g - T_c$ is less than 40 degrees in the dust storm interior. These observations are discussed in the next section.

A number of perturbation studies have been performed on the results in figure 6. In general, the least-squares character of the method makes the solution less sensitive to changes in a single input quantity than the single point inversions of the previous sections. Varying ω_o and β by 10% causes T_g to change by less than 3K, whereas T_c will change less than 6K. Altering the model brightness temperatures T_9, T_{11}, and T_{20}, independently by up to 3 degrees affects T_g less than 1 K, and T_c less than 2K. If T_7 is perturbed while τ_{11C} is less than 3, the change in T_g will be comparable to the size of the perturbation. For $\tau_{11C} > 3$, altering T_7 or the 7 micron extinction coefficient will have an increasingly large effect on T_g. For $\tau_{11C} > 5$, the input parameters do not produce a satisfactory fit to the observed radiances.

In summary, an attempt has been made to set meaningful lit-nits on T_g and T_c based on the assumption that particle properties do not vary between the dust storm surrounding and the interior. T_c is not well constrained by the available data, but it is probably in the lower range of the likely near ground temperatures in the surroundings. Below the storm, T_g must be lower than the ground temperature in the surroundings.

7. DISCUSSION

One of the key questions that may be addressed by studying the thermal structure of a martian local dust storm is whether local thermodynamic effects play an important role in generating the surface shear stress necessary to lift dust. Small, intense convective cells occur in the form of dust devils on Earth, in places where the planetary boundary layer is statically unstable over regions tens to hundreds of meters wide (Ryan and Carroll, 1970). Similar features were found on Mars by the Viking Orbiter cameras (Thomas and Gierasch, 1985). A surface resolution about three orders of magnitude greater than that available in the data of this study would be required to observe these features with infrared imaging. However, the results of the present work suggest that at least over surfaces on the scale of 200 km, vigorous convection at ground level is unlikely in the interior of the dust storm. For the storm studied here, the ground temperature in the storm interior is at least 6K cooler than the ground temperature of the surroundings. Also, thermal contrast between the ground and the atmospheric boundary layer ($T_g - To$) in the storm surroundings at mid afternoon is 30 to 60K over most of the parameter space. From figure 4, the dust storm interior shows this difference to be less than 40K for τ_{11C} between 1 and 3, suggesting that the boundary layer in the cloud region may be more stable

14

against convection than in the surroundings. Both these observations are contrary to expectation for a situation in which direct heating at ground level predominates in the storm interior.

The time evolution of the storm as shown in figure 2 makes the possibility that the convective process operates even at the storm edges appear unlikely. The thermal structure of the storm over regions 200 km in size does not change measurably between 11.5 and 16.6 local hours. If the storm were generated by direct thermal forcing at the ground during part of this period, the static stability would be low at first, and vigorous convection would transport heat and carry dust from the ground (Gierasch and Goody, 1973). In this scenario, the static stability would first decrease in the region of cloud formation as the atmosphere was heated by direct absorption of solar radiation by the dust near the ground. Later, as the dust filled the boundary layer, increased atmospheric heating would cause the static stability to increase. The calculations of this study do not rule out the presence of a region of vigorous convection at the cloud tops, nor the possibility of dust plumes or dust devils on a smaller scale. The observations presented here are more favorable to arguments that the storm is maintained either by the flow of cold air in the form of density currents, or the combined effects of winds forced on scales larger than the size of the storm (Leovy et al., 1973; Pollack et al., 1979). These two hypotheses may be tested when the direction of storm motion can be compared with regional slopes and prevailing winds. Both mechanisms would allow the ground temperature to be relatively cool in the region where dust is being lifted, and neither mechanism is excluded by the apparently unchanging vertical thermal gradient in the boundary layer within the dust storm during the late morning and afternoon.

This study of the Viking IRTM data in the area of one local dust storm led to the conclusion that the dust in the cloud region differs from that observed during the 1971-2 global dust storm observed by Mariner 9. This may be due to differences in the type of dust distributed in regions of the planet, or to selectivity in the mechanisms which lift dust in the two instances. Given the assumptions that the particle scattering (but not extinction) properties are similar to those observed by Mariner 9, and that dust properties do not vary horizontally in the storm region, it is possible to obtain an estimate of the ground temperature and to achieve a crude determination of the atmospheric temperature near the ground within a local dust storm. This technique may be useful in further exploring the thermodynamics of martian dust storms when a more extensive data set is available.

REFERENCES

Binder, A. B., Arvidson, R. E., Guiness, E.A., Jones, K. L., Morris, EC., Mutch, T.A., Pierie, D.C. and Sagan, C., The geology of the Viking lander 1 site. *J. Geophys. Res.* 83, 4439-4451, 1977.

Briggs, G. A., Baum, W.A. and Barnes, J., Viking orbiter imaging observations of dust in the Martian atmosphere. *J. Geophys. Res. 84,2795-2820,* 1979.

Clance, R.P., and S.W. Lee, A new look at dust and clouds in the Mars atmosphere: Analysis of emission-phase -function sequences from global Viking IRTM observations, *Icarus* 93, 135-158, 1991.

Coned, J.E., Infrared emissivities of silicates: experimental results and a cloudy atmosphere model of spectral emission from condensed particulate mediums. *J. Geophys. Res.* 74, 1614-1634, 1969.

Gierasch, P.J. and Goody, R. M., The effect of dust on the temperature of the Martian atmosphere. *J. Atmos. Sci.* 29, 400-402, 1972.

Gierasch, P.J. and Goody, R. M., A study of the thermal and dynamical structure of the Martian lower atmosphere. Planet. Space Sci. 16, 615-646, 1968.

Gierasch, P.J. and Goody, R. M., A model of a Martian great dust storm. *J. Atmos. Sci.* 80, 169-179, 1973.

Greeley, R., Lancaster: N., Lee, S., and Thomas, P., Martian aeolian processes, sediments, and features, in Keiffer, H.H., Jakosky, B. M., Snyder, C. W., and Matthews, M. S., eds., MARS, Univeristy of Arizona Press, 730-766, 1992.

Hess, S.1,., Henry, R. M., Leovy, C.B., Ryan, J.A. and Tillman, J.E., Meteorological results from the surface of Mars: Viking 1 and 2. *J, Geophys. Res.* 82,4559-4574, 1977.

Hovis, W.A. and Callahan, W. R., Infrared reflectance spectra of igneous rocks, tuffs, and red sandstone from 0.5 to 22 microns. *J. Opt. Sot. Am.* 56, 639-643, 1966.

Hunt, G. E., Thermal infrared properties of the Martian atmosphere 4. predictions of the presence of dust and ice clouds from Viking IRTM spectral measurements. *J. Geophys. Res.* 84, 2865-2874, 1979.

Jakosky, B. M., The effects of nonideal surfaces on the derived thermal properties of Mars, *J. Geophys. Res.* 84,8252-8262, 1979.

Kahn, R., Goody, R., and Pollack, J., The Martian twilight. *J. Geophys. Res.* 86,5833-5838, *1981.*

Kahn, R. A., Martin, T. Z., R.W. Zurek, and S.W. Lee, The martian dust cycle, in Keiffer, H. H., Jakosky, B. M., Snyder, C.W., and Matthews, M. S., eds., <u>MARS,</u> Univeristy of Arizona Press, 1017-1053, 1992. .

Kieffer, H. H., Neugebauer, G., Munch, G., Chase, Jr., S.C. and Miner, E., Infrared thermal mapping experiment: the Viking Mars orbiter. *Icarus* 16, 47-56, 1972.

Kieffer, 11.11., Martin, T. Z., Peterfreund, A. R., Jakowsky, B. M., Miner, E.D. and Palluconi, F. D., Thermal and albedo mapping of Mars during the Viking primary mission. *J. Geophys. Res.* 82,4249-4291, 1977.

Leovy, C. B., Zurek, R.W. and Pollack, J. B., Mechanisms for Mars dust storms. *J. Atmos. Sci. .?0,* 749-762, 1973.

Lindzen, R.S. and Kuo, 11.1.., A reliable method for the numerical integration of a large class of ordinary and partial differential equations. *Month. Weath. Rev.* 97,732-734, 1969.

Martin, T.Z., and Kieffer, H. H., Thermal infrared properties of the Martian atmosphere 2: The 15 micron band measurements. *J. Geophys. Res.* 84, 2843-2852, 1979.

Marlin, T. Z., Peterfreund, A. R., Miner, E.D., Kieffer, H.H., and Hunt, G.E., Thermal infrared properties of the Martian atmosphere 1. global behavior at 7,9, 11, and 20 microns. *J. Geophys. Res.* 8-4,2830-2842, 1979.

Moore, I-I. J., Hutton, R. E., Scott, R.F., Spitzer, C.]<., and Shorthill, R. W., Surface materials of the Viking lander sites. *J. Geophys. Res.* 82,4497-4523, 1977.

Murphy et al. 19??

Peterfreund, A. R., and Kieffer, H.H., Thermal infrared properties of the Martian atmosphere 3. local dust storms. *J. Geophys. Res.* 84,2853-2863, 1979.

Pollack, J. B., Colburn, D., Kahn, R., Hunter, J., Van Camp, W., Carlston, C.E., and Wolf, M., Properties of aerosols in the Martian atmosphere as inferred from Viking lander imaging data. *J. Geophys. Res.* 82,4479-4496, 1977.

Pollack, J. B., Colburn, D. S., Flasar, F. M., Kahn, R., Carlston, C. E., and Pidek, D., Properties and effects of dust particles suspended in the Martian atmosphere. *J. Geophys. Res. 84,* 2929-2945, 1979.

Ryan, J. A., and Carroll, J.J., Dust devil wind velocities: mature state. *J. Geophys. Res. 75,531-* 541, 1970.

Ryan, J. A., and Lucich, R. D., Possible dust devils, vortices on Mars. *J Geophys. Res. 88,* 11005-11011, 1983.

Rogers, C. D., Retrieval of atmospheric temperature and composition from remote measurements of thermal radiation. *Rev. Geophys. and Space Phys.* 14, 609-624, 1976.

Sieff, A., and Kirk, D. B., Structure of the atmosphere of Mars on summer at mid latitudes. *J Geophys. Res. 82,4364-4378, 1977.*

Thomas, P. C., and Gierasch, P.J, Dust Devils on Mars, Science 230, 175-177, 1985.

Toon, O.El., Pollack, J. B., and Sagan, C., Physical properties of the particles composing the Martian dust storm of 1971-72. *Icarus* 30,663-696, 1977.

Zurek, R.W., Martian great dust storms: An update. *Icarus* 50,288-310, 1982.

Zurek, R.W., Barnes, J. R., Haberle, R. M., Pollack, J. B., Tillman, J. E., and Leovy, C. B., Dynamics of the martian atmosphere, in Keiffer, H.H., Jakosky, B. M., Snyder, C.W., and Matthews, M. S., eds., <u>MARS</u>, Univeristy of Arizona Press, 835-933, 1992.

APPENDIX

TWO - STREAM RADIATIVE TRANSFER SCHEME

Following Toon et al., 1977, the equation of radiative transfer in a plane parallel atmosphere is written for monochromatic radiation, given the positive direction as upward and optical dept τ as zero at the top:

$$\mu \, dI(\tau,\mu,\theta) \, / \, d\tau = I(\tau,\mu,\theta) - J(\tau,\mu,\theta) \tag{1}$$

where I in the intensity, μ the cosine of the emission angle, θ is the scattering angle, and J is the source function. In the 2-stream approximation:

$$-\frac{1}{\sqrt{3}} \, df \, / \, d\tau = f - J^{+} \tag{2}$$

$$-\frac{1}{\sqrt{3}} \, df \, / \, d\tau = g - J^{-} \tag{3}$$

Here f and g are the upward and downward 2-stream intensities, respectively.

$$J^{+} = \tilde{\omega}_o/2 \, (1+\beta) f - t \, \tilde{\omega}_o/2 \, (1-\beta) g + (1-\tilde{\omega}_o) B_\nu(\tau) \tag{4}$$

With $B_\nu(\tau)$ as the Planck function at frequency v for the temperature at atmospheric level τ, and

$$J^{-} = \tilde{\omega}_o/2 \, (1+\beta) g + \tilde{\omega}_o/2 \, (1-\beta) f + (1-\tilde{\omega}_o) B_\nu(\tau) \tag{5}$$

Rewriting equations (2) and (3) using (4) and (5):

$$f' = af - bg - c \tag{6}$$

$$g' = - ag + bf + c \tag{7}$$

where:

$$a = \sqrt{3}\left(1 - \tilde{\omega}_o/2\left(1+\beta\right)\right)$$

$$b = \sqrt{3}/2\,\tilde{\omega}_o\left(1-\beta\right) \tag{8}$$

$$c = \sqrt{3}\left(1-\tilde{\omega}_o\right)B_v(\tau)$$

$\tilde{\omega}_o$ and β are the single scattering properties discussed in the text. By cross-differentiating equations (6) and (7), a second order differential equation for f is obtained:

$$f'' + (b'/\ b)\ f' + \left(b^2 - a^2\right) + a/b\ b' - a'\right)f = c/b\ b' - (a+b)c - c'$$

where primes are derivatives with respect to τ. When the particle properties are constant over the whole atmosphere, this equation reduces to:

$$f' + \left(b^2 - a^2\right)f = -(a+b)c - c' \tag{9}$$

The lower boundary condition is

$$f(\tau^*) = \varepsilon B_v(T_g) \tag{lo}$$

where τ^* is the total atmospheric opacity and ε is the ground emissivity. "l'he boundary condition at the top of the atmospheres chosen as:

$$g(0) = o \tag{11}$$

Using (2), the upper boundary condition becomes:

$$f'(0) -- af + c = O \tag{12}$$

The solution to (9), with (10) and *(12), is* obtained using the method of Lindzen and Kuo (1969). Then g is obtained as an initial value problem using a Runge-Kutta method with (11) as the initial value. The solution to the equation of radiative transfer for the upward intensity is:

$$f(0) = \varepsilon B_v(T_g)e^{-\frac{\tau^*}{\mu}} + \int_0^{\tau^*} e^{-\frac{t}{\mu}}\ J(t)\,dt/\mu \tag{13}$$

20

where J(t) is the source function. J(t) is replaced with the source function in the upward direction J' from equation (4), and the integration is performed numerical y to obtain the emergent intensity. Contributions from atmospheric gasses are neglected. The CO_2 opacity averaged over the 7, 9, 11, or 20 micron IRTM passbands is at least three orders of magnitude less than the observed opacity in these bands for a 7 mb atmosphere.

FIGURE CAPTIONS

Figure 1:   I RIM passbands, from Kieffer_et_al, 1977.

Figure 2: JRTM Dust Storm Data. Each traverse contains data from a latitude strip 3 to 4 degrees wide. Temperature differences and the 11 micron brightness temperature are plotted as functions of longitude for the four IRTM sequences. Sequence 210180 was taken at 11.5 local hours, with a surface resolution of 220 km, 210181 is at 12.8 local hours and 230 km resolution, 210182 at 14.6 local hours and 230 km resolution, and 210183 at 16.6 local hours and 225 km resolution.
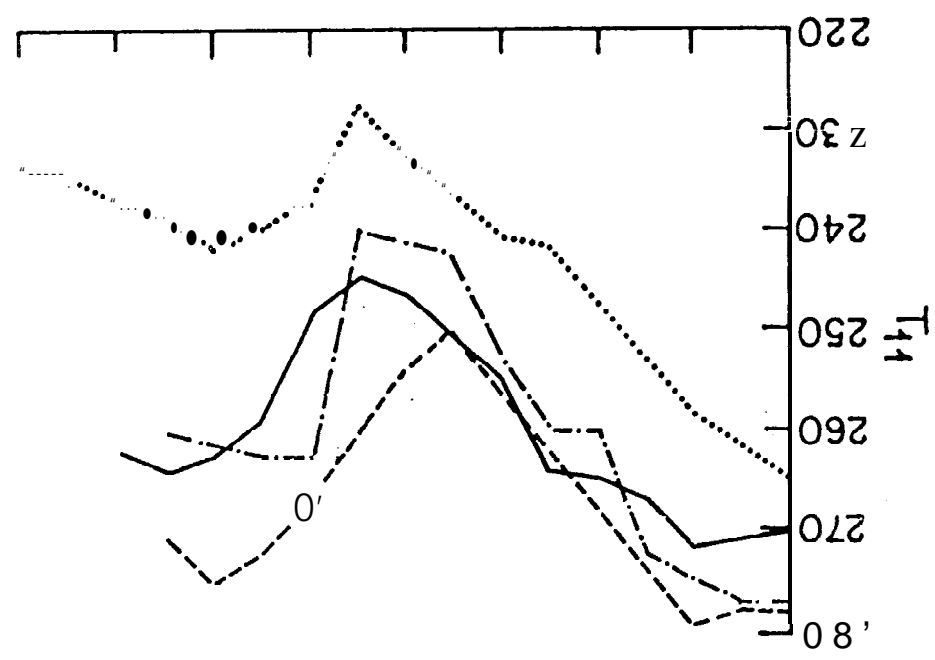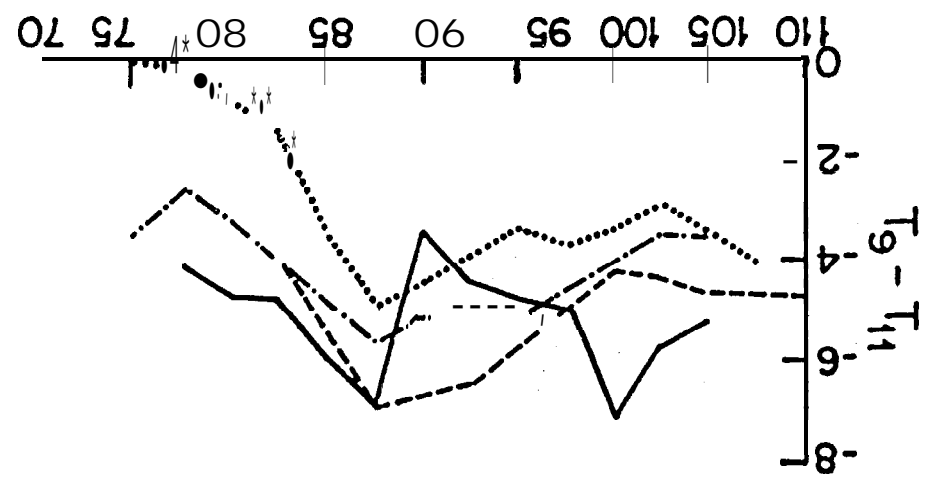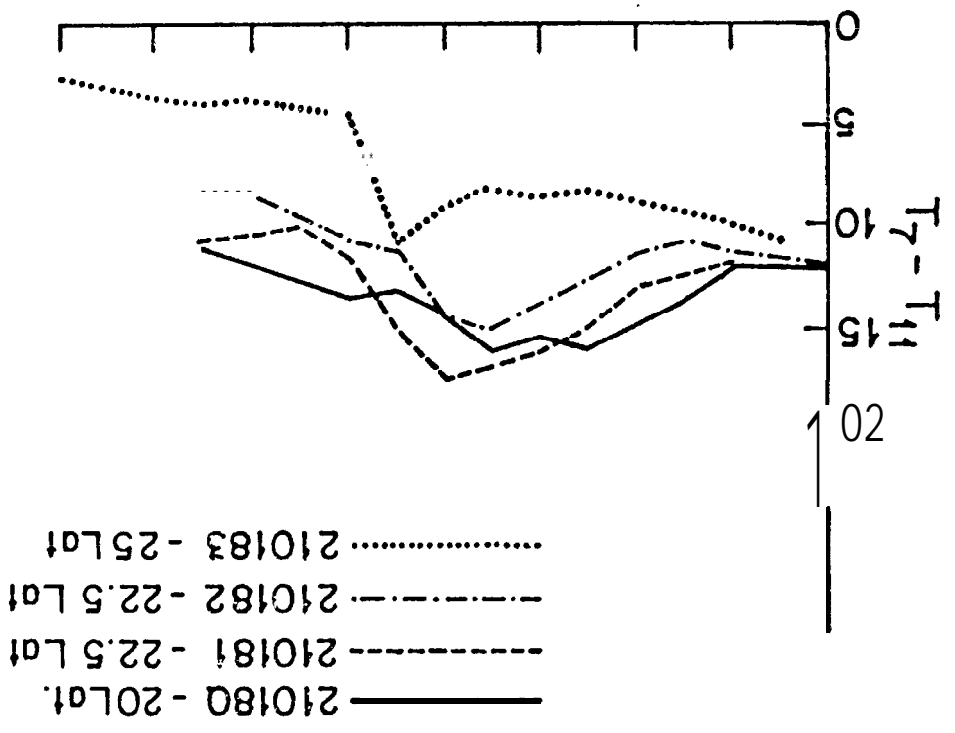
Figure 3: Parameters for model thermal profiles. (a) Model parameters for atmospheric temperature structure. Here $1_{BL} = (T_0 - T_{BL})/z_{BL}$, and $1-a = (T_{BL} - T_{TROP}) / (z_{TROP} - z_{BL})$. (b) Model parameters for dust storm interior temperature structure.
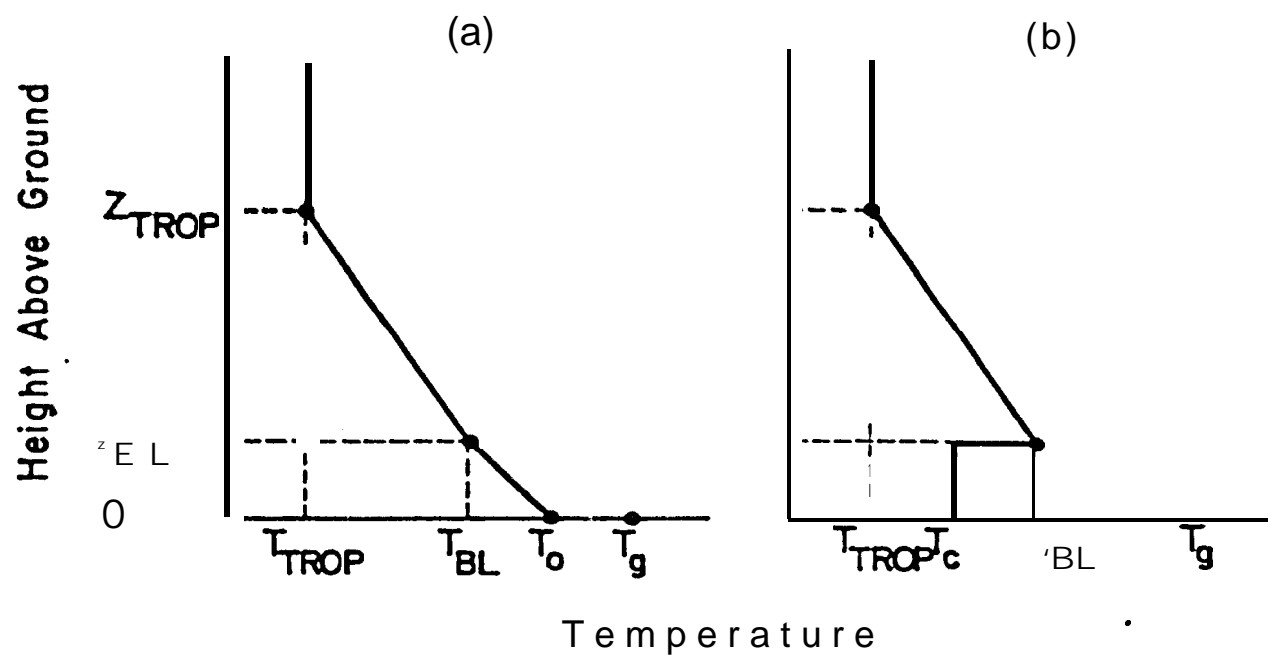
Figure 4: IRTM Dust Storm Surroundings Models. Derived ratios of extinction coefficients are plotted against the atmospheric temperature T_O for three choices of T_g and two choices of Γ_{BL}. z_{TROP} was fixed at 50 km, and T_{24} at 200K for all cases. Circles show the corresponding ratios for Mariner 9 dust particles.
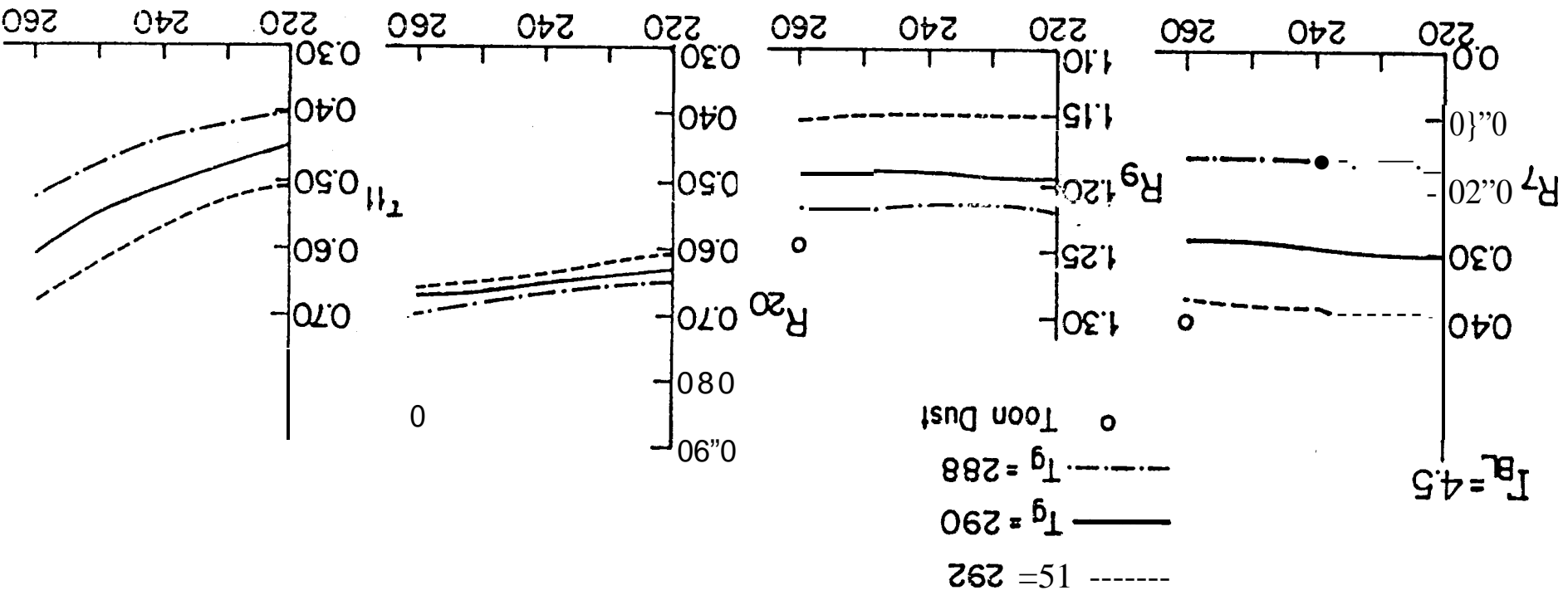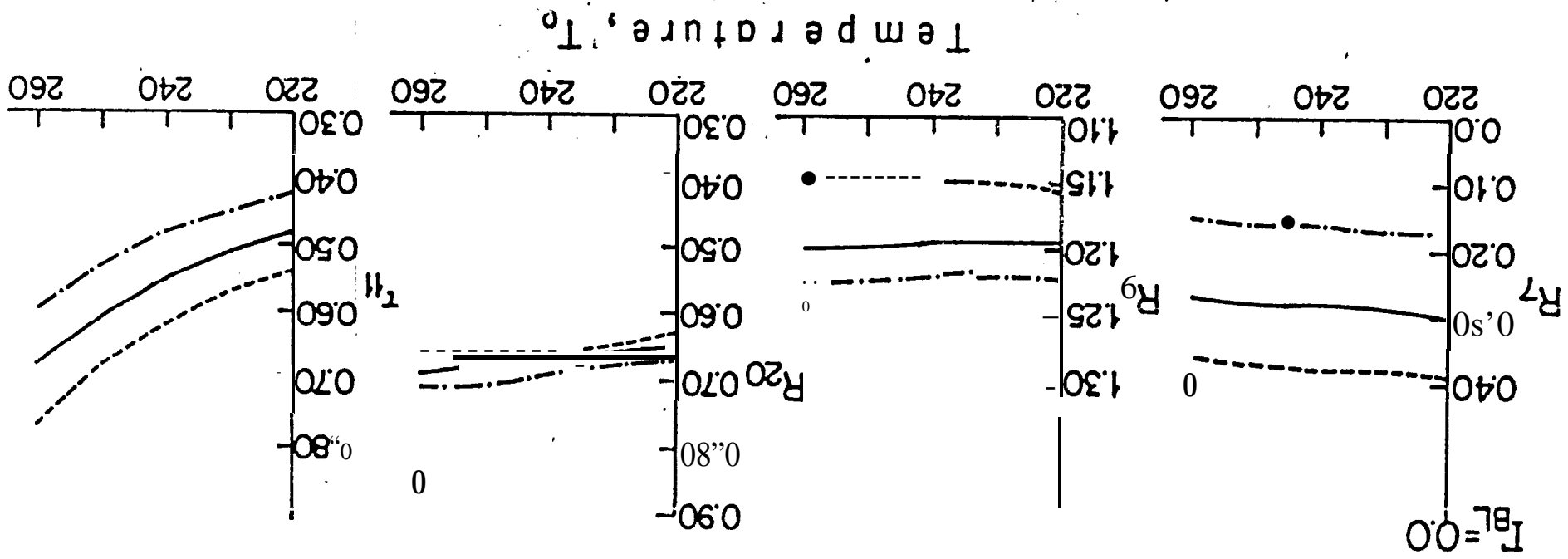
Figure 5: Viking Lander 1 Site Models. Ratios of extinction coefficients and the 11 micron optical depth are plotted as functions of ground temperature for a model in which the atmospheric temperature is derived from in situ measurements taken during spacecraft landing. Symbols show the corresponding ratios for Mariner 9 dust particles.

Figure 6: Dust Storm Interior Model. Ground temperature (upper) and cloud temperature (lower) are plotted as functions of the 11 micron dust cloud opacity. The dust strom top is fixed at 4 km, and the 11 micron opacity above 4 km is set to 0.4. $T_{4 km}$ is set at 220K and $T_{24 km} = 200K$.

(a) (b)

Height Above Ground
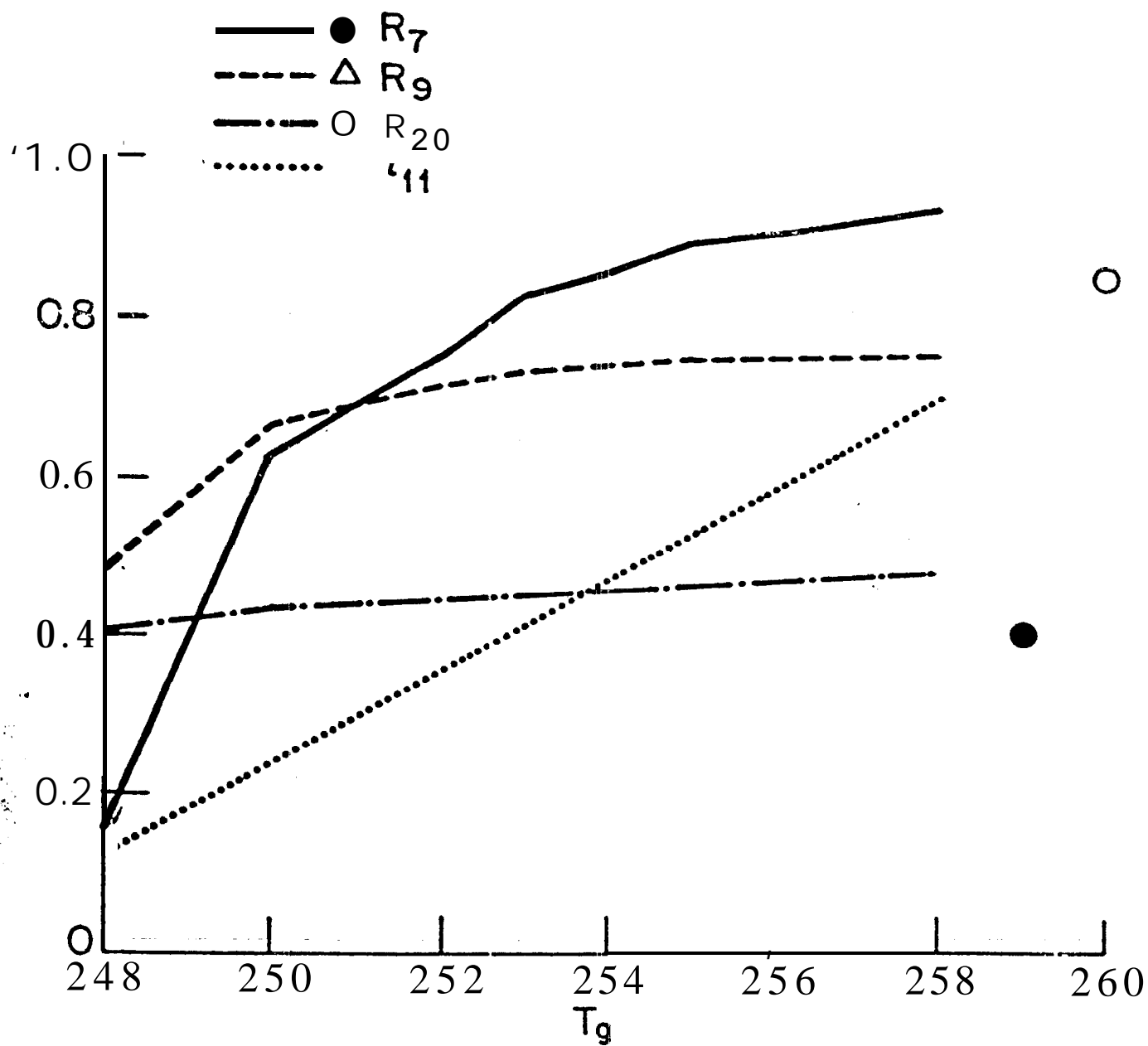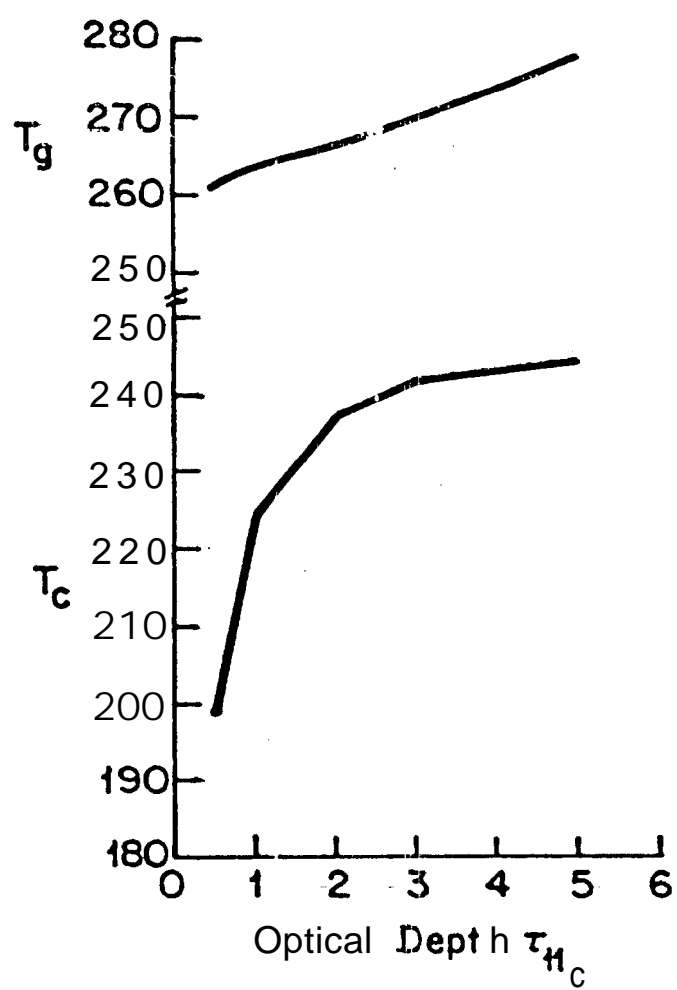
Temperature

A

Legend:
- ● R_7 (solid line)
- △ R_9 (dashed line)
- ○ R_{20} (dash-dot line)
- t_{11} (dotted line)

Y-axis: '1.0, 0.8, 0.6, 0.4, 0.2, O

X-axis: T_9 — 248, 250, 252, 254, 256, 258, 260

Optical Depth τ_{H_c}
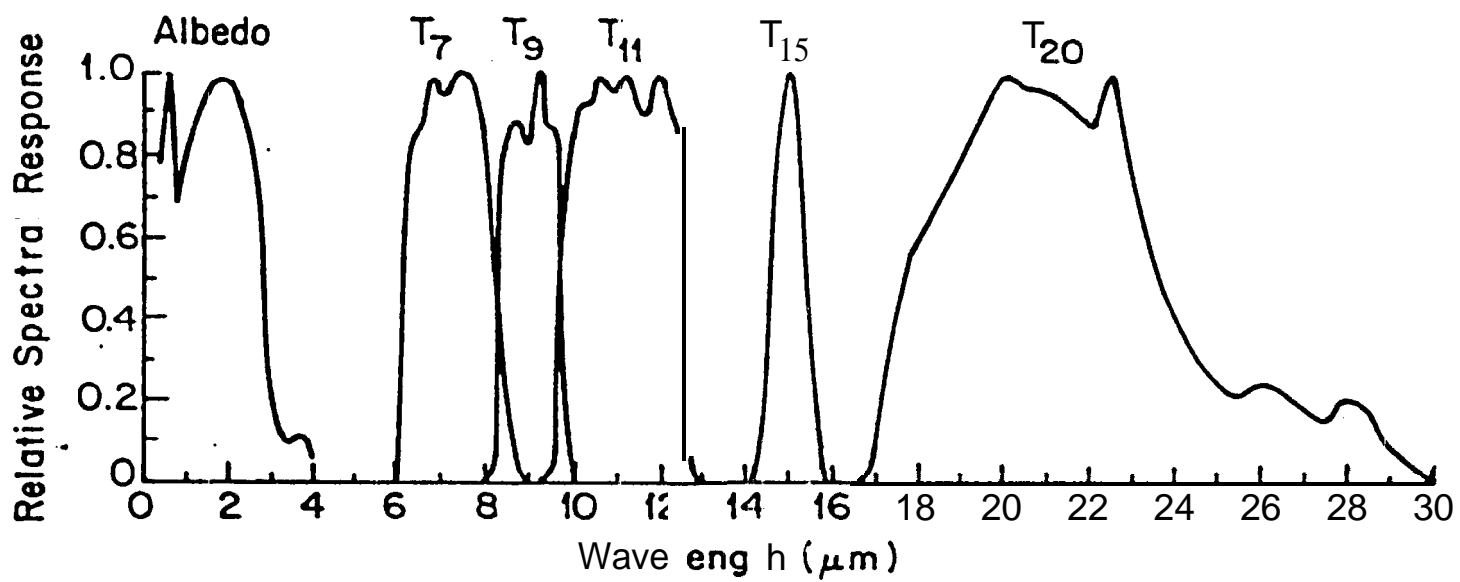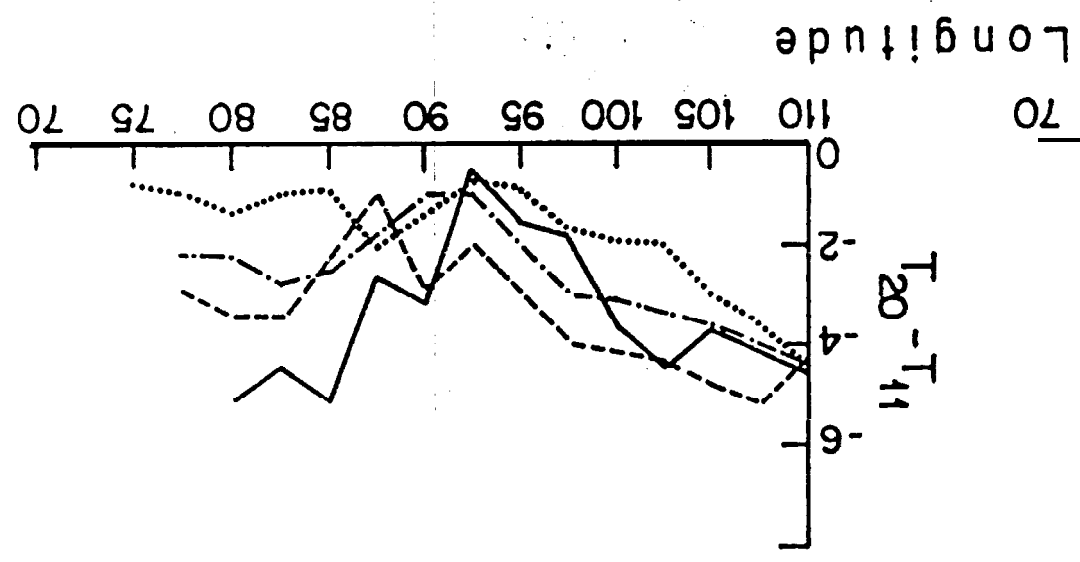
Table 1
Representative Dust Storm Thermal Signature

	Storm Center	Storm Surroundings
$T_7 - T_{11}$	16.	11.
$T_9 - T_{11}$	-7.	-5.
$T_{20} - T_{11}$	0.10-2.	-4.
T_{11}	240.	2.75.

Table 2.
IRTM Channel-Mean-Weighted Properties at T = 220K for Dust Observed by Mariner 9
(Toon et al., 197?)

	7 micron	9 micron	11 micron	20 micron
$Q_e(cm^2)$	4.88×10^{-8}	1.49×10^{-7}	1.21×10^{-7}	1.04×10^{-7}
ω_o	0.453	0.432	0.636	0.351
β	*0.780*	*0.506*	*0.559*	*0.318*

"Table 3
Particle Extinction Coefficient Ratios

	Dust Storm Surroundng	Mariner 9
R_7	*0.29 (+.11, -.25)*	0.403
R_9	1.18 (±.06)	1.24
R_{20}	0.67 (±.04)	0.860

Table 4
VL1 Site Data Summary Giving Mean and Standrad Deviation for the 11 Micron Brightness Temperature and
Spectral Brightness Temperature Differences

Revolution/ Sequence	Emission Angle	Local Hour	Resolution (km)	T_{11}	T_7-T_{11}	T_9-T_{11}	$T_{20}-T_{11}$
20/105	27.7	15.39	10.7	248.6 (.78)	2.55 (.35)	1.07 (.06)	.57 (.31)
20/106	17.1	15.49	**9.0**	245.6 (.43)	2.40 (.26)	1.07 (.15)	.73 (.28)
20/107	17.5	15.57	8.8	245.0 (.49)	2.10 (.10)	0.87 (.23)	.52 (.45)
27/102	19.1	15.90	9.1	243.1 (.35)	2.07 (.12)	1.20 **(.20)**	**.90 (.49)**
27/103	5.6	15.94	**8.1**	**242.9 (.97)**	**1.97 (.25)**	**1.03 (.?3)**	**.21 (.43)**
27/104	16.3	15.98	8.4	241.7 (.77)	1.73 (.12)	1.17 (.15)	.63 (.50)
27/105	30.3	16.00	10.0	240.8 (.67)	1.87 (.21)	0.67 (.50)	.44 (.59)
35/128	40.5	15.62	13.8	247.5 (.46)	3.23 (.45)	2.30 (.42)	3.1 (.23)
35/129	31.2	15.65	11.0	247.4 (.79)	2.20 (.17)	1.50 (.10)	.34 (.22)
37/1 13	23.0	15.61	9.5	248.2 (.37)	2.13 (.15)	1.67 (.15)	.67 (.25)

Table 5

Viking Lander 1 Site Mid-Afternoon Spectral Brightness Temperature Differences, Near Sol O

Temperature Difference	(K)
$T_7 - T_{11}$	2.0
$T_9 - T_{11}$	1.0
$T_{20} - T_{11}$	0.5
T_{11}	245.8